APL Photonics

High-order cylindrical vector beams with tunable topological charge up to 14 directly generated from a microchip laser with high beam quality and high efficiency

Cite as: APL Photonics 4, 106106 (2019); https://doi.org/10.1063/1.5119789
Submitted: 12 July 2019 . Accepted: 24 September 2019 . Published Online: 09 October 2019

Dimeng Chen, Yujie Miao, Hao Fu, Hongsen He, Jia Tong, and Jun Dong

High-order cylindrical vector beams with tunable topological charge up to 14 directly generated from a microchip laser with high beam quality and high efficiency

Cite as: APL Photon. 4, 106106 (2019); doi: 10.1063/1.5119789
Submitted: 12 July 2019 • Accepted: 24 September 2019 •
Published Online: 9 October 2019

Dimeng Chen,[1] Yujie Miao,[1] Hao Fu,[2] Hongsen He,[1] Jia Tong,[1] and Jun Dong[1,a)]

AFFILIATIONS

[1]Laboratory of Laser and Applied Photonics (LLAP), Department of Electronic Engineering, School of Electronic Science and Engineering, Xiamen University, Xiamen 361005, China
[2]Department of Software Engineering, Xiamen University, Xiamen 361005, China

[a)]**Author to whom correspondence should be addressed:** jdong@xmu.edu.cn

ABSTRACT

Large topological charge optical vortex beams carrying orbital angular momentum have potential applications on optical trapping, optical communication with high capacity, quantum information processing. However, the beam quality is degraded in vortex beams generated with spiral phase plates or resonator mirrors with defect spots and optical conversion efficiency in solid-state lasers is sacrificed by controlling the loss of resonator. It is a big challenge for generating high beam quality, high-order cylindrical vector beams with large topological charge in compact solid-state lasers. Here, high-order cylindrical vector beams [Laguerre-Gaussian (LG) modes with zero degree and order of l, $LG_{0,l}$] with tunable topological charges up to 14 have been generated in an annular beam pumped Yb:YAG microchip laser by manipulating the pump power-dependent population inversion distribution. Efficient performance with optical efficiency of 17.5% has been achieved. The output power is 1.36 W for a vector-vortex laser with 14 topological charges. The pump power dependent wavelength tunable and dual-wavelength laser oscillation in vector-vortex beams has been observed by controlling the reabsorption loss at 1030 nm. Wavelength tunable, dual-wavelength (1030 and 1050 nm) laser oscillation has been achieved for vector-vortex beams with topological charges of 8, 9, and 10. The laser beam quality factor M^2 close to the theoretical value $(l + 1)$ has been achieved for $LG_{0,l}$ vector-vortex beams with tunable topological charges up to 14. This work provides a new effective method for generating large topological charge high-order cylindrical vector beams in solid-state microchip lasers with high efficiency and high beam quality.

I. INTRODUCTION

Large topological charge vector-vortex laser beams have been demonstrated for potential applications on high capacity storage,[1] information processing,[2] quantum entanglement,[3] high resolution imaging,[4] and optical manipulation.[5] Laguerre-Gaussian (LG) modes with zero degree and order of l ($LG_{0,l}$) are ideal vortices and possess unique properties of intensity zero along the beam axis and helical phase, especially carrying orbital angular momentum (OAM).[6] Besides unique properties of amplitude and phase, the inhomogeneous polarization states of $LG_{0,l}$ vector-vortex beams (one class of the high-order cylindrical vector beams) provide more flexibilities for various potential applications such as tightly focusing, imaging, and optical communications.[7–9] Various methods have been proposed to generate vector-vortex beams. Traditionally, the spatial light modulator (SLM),[3] spiral phase plate (SPP),[10] and hologram formed with liquid crystal[11] have been used to generate specially designed vortex beams in the extra-cavity laser scheme. High-order cylindrical vector beams have been demonstrated experimentally by interferometrically superposing two opposite circular-polarized LG beams.[12] However, the propagation of these vortex beams is unstable owing to the imperfections of phase element

processing.[13] The achieved power and optical efficiency are low because of the low damage thresholds of these optical elements made from liquid crystals. Vector-vortex beams with a Bessel-Gaussian profile have been investigated theoretically under the rigorous vector electromagnetic analysis.[14] The discrete main spots in the focal plane have been obtained by tightly focusing vector-vortex Bessel-Gaussian beams with $n \neq 1$. Vector-vortex beams have been generated successfully in a laser by using mode selecting elements inside the cavity such as birefringent elements,[15,16] conical Brewster prism,[17] and polarization selective end mirror devices.[18] Resonator mirrors with a defect spot[19] or inscribed round patterns[20] have been utilized to generate vortices with large topological charges. Vector-vortex beams with topological charge from 1 to 8 were obtained in a Nd:YAG laser by applying a spot-defect mirror.[19] Optical vortex with topological charges up to 288 has been achieved in a Nd:YVO_4 laser by adopting output coupling mirror inscribed round patterns.[20] The output power and optical efficiency that from these lasers are limited because more losses are introduced with defects designed on the cavity mirror or output coupler (OC). Especially, the transition from one vortex to another high topological charge vortex has to precisely adjust the defect size on the output coupler and increase pump power to overcome the lasing threshold. Annular beam pumping has been demonstrated to be an effective method in the end-pumped solid-state laser for generating vortices.[21] Annular beams have been formed from a fiber-coupled laser-diode with mode-converting fiber,[21,22] axicon,[23] and hollow focus lens.[24] However, conversion efficiency from fiber-coupled laser-diode with the Gaussian profile to an annular beam is low because some part of the pump power has to be sacrificed and extra diffraction loss is introduced with mode conversion elements. The annular beam formed by direct beam shaping of a fiber-coupled laser-diode has been used to pump a Yb:YAG microchip laser for generating $LG_{0,1}$ vector-vortex beams with tunable polarization states.[25] High power and highly efficient vector-vortex lasers with different polarization states have been achieved in an annular beam pumped Yb:YAG microchip laser. Compared to Nd^{3+}-doped laser materials, ytterbium ions (Yb^{3+}) doped laser materials especially Yb:YAG crystals are ideal candidates of solid-state lasers for achieving large topological charge vector-vortex lasers with high power and high efficiency because they have remarkable properties such as low quantum defects, broad absorption and emission spectra, and high doping concentration.[26,27] Therefore, it is worth investigating annular beam pumped Yb:YAG microchip lasers for generating high beam quality, large topological charge $LG_{0,l}$ vector-vortex beams with spatial polarization distribution in a form of $\boldsymbol{E}_{0,l}(\phi) = \boldsymbol{E_x}\cos(l\phi) + \boldsymbol{E_y}\sin(l\phi)$,[28] where l is the topological charge and $\boldsymbol{E_x}$ and $\boldsymbol{E_y}$ are the unit vectors in the Cartesian coordinate system.

Here, we reported on generation of high-order cylindrical vector beams with tunable topological charge directly from a Yb:YAG microchip laser under annular beam pumping. An optical vortex with topological charges of 14 has been directly generated by increasing the pump power. High beam quality has been confirmed for the vector-vortex beams with tunable topological charge, l, by measuring the beam quality factor, M^2, which is close to the theoretically predicted value of $l + 1$. Vector-vortex beams with wavelength tunable from 1030 nm to 1050 nm and dual-wavelength (1030 and 1050 nm) operation have been observed depending on the applied pump power. The output power was measured to be 1.36 W for the vector-vortex laser with a topological charge of 14 and optical efficiency was as high as 17.5%.

II. THEORETICAL MODELING

The annular beam from a fiber-coupled laser-diode was collimated and focused with an optical system composited of two lenses with different focal lengths. The focused annular pump beam can be expressed as a superposition of fundamental TEM_{00} mode lasers with a z-dependent separation of r_0. The normalized pump power distribution of the focused annular pump beam is as follows:[25]

$$R_p(r,z) = \frac{\alpha}{\pi w_p^2(z)} \frac{\exp(-\alpha z)}{[1-\exp(-\alpha L_c)]} \times \left[\exp\left(\frac{-2(r-r_0)^2}{w_p^2(z)}\right) + \exp\left(\frac{-2(r+r_0)^2}{w_p^2(z)}\right)\right], \quad (1)$$

where α is the absorption coefficient of the laser crystal at the pump wavelength, L_c is the length of the laser crystal, $w_p(z)$ is the beam radius of the TEM_{00} mode along the beam propagation direction, r_0 is the distance between the beam axis and the position of the TEM_{00} mode at the maximum intensity and can be expressed as $r_0 = |z - z_0|\tan(\theta_p)$, θ_p is the far-field half-angle, and z_0 is the focal position of the pump beam.

By considering the pump power intensity saturation effect, the saturated population inversion in laser crystal induced by the focused annular beam can be expressed as

$$\Delta N(r,z) = \frac{P_{in}\left(1-e^{-\alpha L_c}\right)R_p(r,z)\tau - N_1^0}{h\nu_p\left(1+\frac{I_p(r,z)}{I_s}\right)}, \quad (2)$$

$$I_p(r,z) = \frac{P_{in}e^{-\alpha z}}{\pi w_p^2(z)}\exp\left(\frac{-2r^2}{w_p^2(z)}\right), \quad (3)$$

where P_{in} is the incident pump power, I_s is the saturated pump power intensity, $I_p(r, z)$ is the pump power intensity distribution along the pump beam axis, and $N_1{}^0$ is the population at the low laser level, which depends on the temperature of the laser crystal and is responsible for the reabsorption loss of the Yb:YAG crystal at a lasing wavelength of 1030 nm.

Formation of the laser mode in solid-state lasers is determined by the population inversion distribution in the gain medium. For the end-pumped microchip laser, the absorbed pump power decays exponentially along the thickness of gain medium. Therefore, the position-dependent population inversion excited by the absorbed pump power cannot fully be used for explaining the oscillation of laser modes. The effective saturated population inversion, defined as averaged population inversion along the thickness of gain medium, can be used to illustrate the overlap between laser mode and population inversion distribution. For the annular beam pumped Yb:YAG microchip laser, owing to the short laser gain medium, the effective saturated population inversion in the Yb:YAG microchip laser can be expressed as

$$\Delta N_{eff}(x,y) = \frac{\int_0^{L_c}\Delta N(x,y,z)dz}{L_c}. \quad (4)$$

The $LG_{0,l}$ vortex laser mode is preferable to oscillate under annular beam pumping because the optimum mode overlap is

achieved between the $LG_{0,l}$ mode laser and annular pump beam. The normalized $LG_{0,l}$ mode intensity distribution, $s_{0l}(r, \phi, z)$, can be expressed as

$$s_{0l}(r,\phi,z) = \frac{2}{\pi w_0^2 L_c}\frac{1}{l!}\left(\frac{2r^2}{w_0^2}\right)^l \exp\left(\frac{-2r^2}{w_0^2}\right), \quad (5)$$

where the variation of $s_{0l}(r, \phi, z)$ along propagation direction, z, is neglected, and laser beam waist, w_0, is assumed to be constant along the laser propagation direction inside the laser cavity.

For a focused annular beam end-pumped Yb:YAG microchip laser, the threshold pump power ($P_{th,l}$) for a single $LG_{0,l}$ mode oscillation can be expressed as[29]

$$P_{th,l} = \frac{h\nu_p Loss_{c,l}}{2\sigma L_c \tau \eta_a}\frac{1}{\iiint s_{0l}(r,\phi,z)R_p(r,z)dV}, \quad (6)$$

where τ and σ are is the fluorescence lifetime and emission cross section of the Yb:YAG crystal, L_c is the crystal length, η_a is the absorption efficiency, h is the Planck constant,ν_p is the pump frequency, $Loss_{c,l}$ is the round-trip cavity loss of the $LG_{0,l}$ mode including diffraction loss of the $LG_{0,l}$ mode,[30] the transmission loss of the cavity mirrors, and reabsorption loss at lasing wavelength. Therefore, $Loss_{c,l}$ can be expressed as follows:[30]

$$Loss_{c,l} = 8k_{0l}^2\frac{\delta(M+\delta)}{\left[(M+\delta)^2+\delta^2\right]^2} + \ln\left(\frac{1}{R}\right) + \alpha_L L_c\sqrt{8l}, \quad (7)$$

where k_{0l} is the lth zero of the Bessel function of order l, $\delta = 0.824$, $M = (8\pi N)^{0.5}$, N is the Fresnel number, $N = a^2/\lambda L$, a is the aperture of the mirror, L_c is the crystal length, λ is the laser wavelength, α_L is the absorption coefficient at lasing wavelength, and R is the reflectivity of output coupler.

III. EXPERIMENTS

Figure 1(a) shows the schematic of the annular beam end-pumped Yb:YAG microchip laser for generating vector-vortex beams with tunable topological charges. The pump source was a fiber-coupled laser-diode working at 940 nm. The output beam profile was annular as shown in Fig. 1(b), which was achieved by arranging two groups light emitters unevenly inside the diode bar, combining with total-reflection effect of a multimode fiber. The annular pump beam was random polarized, as shown in Fig. 1(c). With two lenses (f = 8 mm), the annular pump beam was focused. The radius of the focal spot was measured to be 20 μm, and the beam divergence angle was about 10°. The gain medium is a ϕ10 mm × 1 mm Yb:YAG crystal (10 at.% Yb^{3+} doping concentration). The microchip laser was constructed by tightly attaching coated Yb:YAG crystal and output coupler (OC). One surface of the Yb:YAG crystal coated with high reflection (HR) at 1030–1060 nm and antireflection (AR) at 940 nm acts as the rear cavity mirror (M1). AR was coated on other surface of the Yb:YAG crystal to further reduce intracavity losses. OC is a plane-parallel mirror (reflectivity is 98% at 1030–1060 nm). High reflectivity of the OC ensures the high order modes oscillation in the microchip laser cavity. Based on the focus spot position dependent polarization states achieved in the Yb:YAG microchip laser,[25] the vector-vortex beams were generated by setting the focal spot 0.4 mm inside the Yb:YAG crystal to control the Gouy phase.[31] The intensity profiles of the output vector-vortex laser beams were recorded with a beam profile analyzer. The laser spectra were measured with an optical spectral analyzer (Anritsu, MS9740A, resolution is 0.03 nm).

IV. RESULTS AND DISCUSSION

A. High beam quality $LG_{0,l}$ vortex beams with tunable topological charges

The threshold pump power (P_{th}) of the annular beam pumped Yb:YAG microchip laser was 1.85 W. The output transverse intensity profiles were measured with a beam profile analyzer, and the donut-shaped transverse profiles were obtained when the incident pump power was higher than P_{th}. The obtained donut-shaped transverse profiles were fitted theoretically with $LG_{0,l}$ expressions and found that the output donut-shaped transverse profiles were $LG_{0,l}$

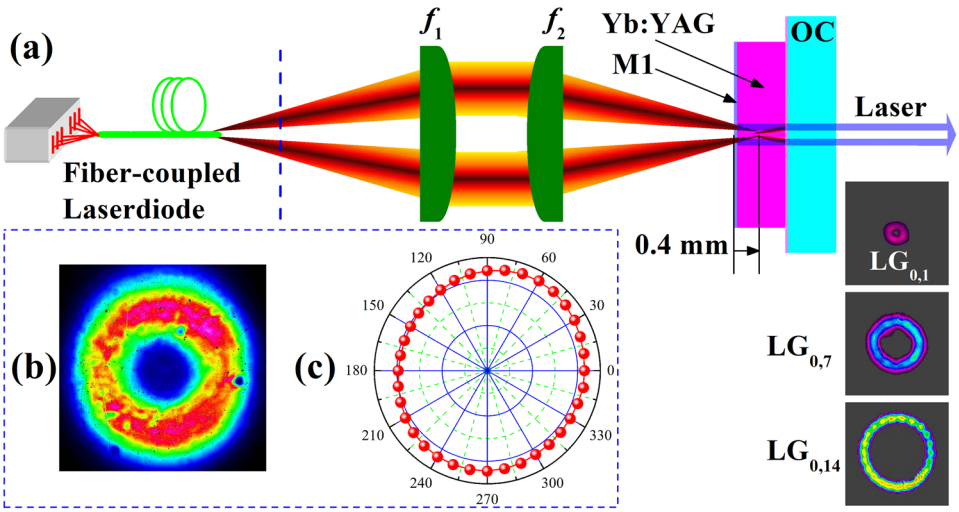

FIG. 1. (a) Experimental setup of the annular beam end-pumped Yb:YAG microchip laser for directly generating high-order cylindrical vector beams with tunable topological charge. f_1 is the collimating lens, and f_2 is the focus lens. M1 is the rear cavity mirror coated with AR at 940 nm and HR at 1030–1060 nm. OC is the output coupler. (b) Beam intensity profile of the annular laser beam emitting from the fiber. (c) Measured polarization state of the annular pump laser beam.

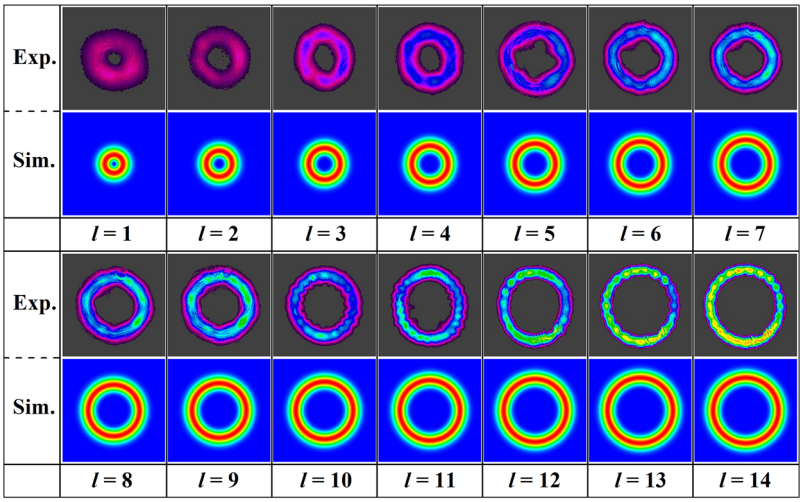

FIG. 2. Experimentally obtained transverse intensity profiles generated in an annular beam pumped Yb:YAG microchip laser and theoretically simulated transverse intensity profiles with the $LG_{0,l}$ expressions (l = 1, 2, . . ., 14). The corresponding input pump powers are P_{in} = 2.1 W, 2.9 W, 3.5 W, 3.8 W, 4.2 W, 4.4 W, 4.8 W, 5.2 W, 5.7 W, 6.1 W, 6.5 W, 7 W, 7.5 W, and 7.8 W.

modes with the order of l from 1 to 14 depending on the applied pump power. The $LG_{0,1}$ mode was obtained when P_{in} was higher than P_{th}. The $LG_{0,2}$ mode laser oscillated when P_{in} was higher than 2.85 W. The $LG_{0,3}$ mode laser oscillated when P_{in} was in the range from 3.32 W to 3.7 W. The threshold pump powers were 3.7 W, 4 W, 4.32 W, and 4.61 W for $LG_{0,4}$, $LG_{0,5}$, $LG_{0,6}$, and $LG_{0,7}$ mode lasers, respectively. Further increasing P_{in} to 5.08 W, the $LG_{0,8}$ mode laser oscillated. The $LG_{0,9}$ mode laser oscillated when P_{in} was higher than 5.55 W, and the $LG_{0,10}$ mode laser oscillated when P_{in} was higher than 5.94 W. The threshold pump powers were 6.41, 6.9, 7.35, and 7.73 W for $LG_{0,11}$, $LG_{0,12}$, $LG_{0,13}$, and $LG_{0,14}$ mode lasers, respectively. Figure 2 shows measured donut-shaped intensity profiles oscillated in $LG_{0,l}$ modes with order l from 1 to 14 at different P_{in}s, together with the theoretical simulated transverse intensity profiles with the $LG_{0,l}$ expression. The output donut-shaped laser transverse profiles are kept, and the inner diameter of donut-shaped laser transverse intensity profiles increases with P_{in}. The switch from one $LG_{0,l}$ ($l \geq 1$) mode to the adjacent $LG_{0,l+1}$ mode was abrupt when P_{in} was high enough to overcome the lasing threshold of the $LG_{0,l+1}$ mode.

The purity of all the $LG_{0,l}$ modes generated in the microchip laser was double checked by carefully fitting the transverse intensity profile along the x-axis with $LG_{0,l}$ expressions. Figure 3 shows some typical measured transverse intensity profiles of donut-shaped lasers along the x-axis and theoretically simulated curves with $LG_{0,l}$ expressions. The intensity distribution profile of the donut-shaped laser at P_{in} = 2.1 W is fitted well with the curve calculated with $LG_{0,1}$ expression, as shown in Fig. 3(a). The transverse profile at P_{in} = 4.2 W is fitted pretty well with the $LG_{0,5}$ expression, as shown in Fig. 3(b). The transverse profiles obtained at P_{in} = 6.5 W and P_{in} = 7.8 W are in good agreement with the curves calculated with $LG_{0,10}$ and $LG_{0,14}$ expressions, as shown in Figs. 3(c) and 3(d), respectively. As shown in Figs. 2 and 3, the experimentally obtained transverse profiles at different P_{in}s are in good agreement with theoretical simulation with $LG_{0,l}$ expressions, which clearly confirms that pure $LG_{0,l}$ mode laser oscillation has been achieved in the annular beam pumped Yb:YAG microchip laser depending on applied pump power.

Oscillation of $LG_{0,l}$ modes in the annular beam pumped Yb:YAG microchip laser is attributed to the pump power-dependent population inversion distribution inside the Yb:YAG crystal. Based on the annular beam pumping condition (as shown in Fig. 1), the saturated population inversion distribution inside the Yb:YAG crystal and effective saturated population inversion distribution were calculated according to Eqs. (2) and (4), respectively. The parameters used in the theoretical calculations are $\alpha = 10\ cm^{-1}$, $w_{p0} = 20\ \mu m$, $\theta_p = 10°$, $L_c = 1$ mm, and $z_0 = 0.4$ mm. The theoretically calculated population inversion distribution along the crystal length and radius of the Yb:YAG crystal at different incident pump powers is shown in Figs. 4(a1)–4(d1). The pumped areas with population inversion higher than $4 \times 10^{20}\ cm^{-3}$ and $8 \times 10^{20}\ cm^{-3}$ are shown with red and black contour lines in Figs. 4(a1)–4(d1) for comparing the effect

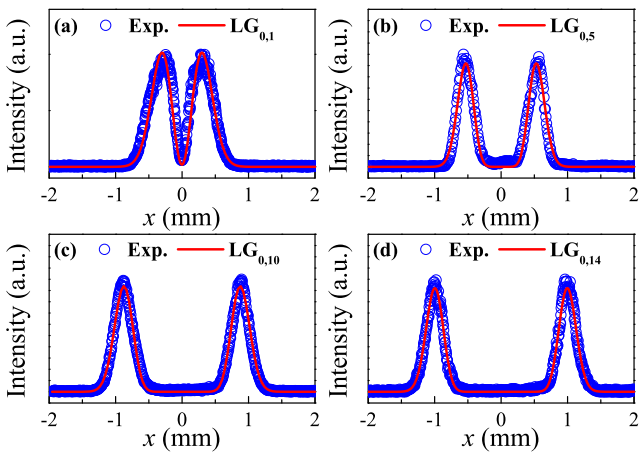

FIG. 3. Measured transverse intensity profiles along the x-axis at (a) P_{in} = 2.1 W, (b) P_{in} = 4.2 W, (c) P_{in} = 6.1 W, and (d) P_{in} = 7.8 W in an annular beam pumped Yb:YAG microchip laser. Solid lines are theoretical simulations with the $LG_{0,l}$ expression (l = 1, 5, 10, 14).

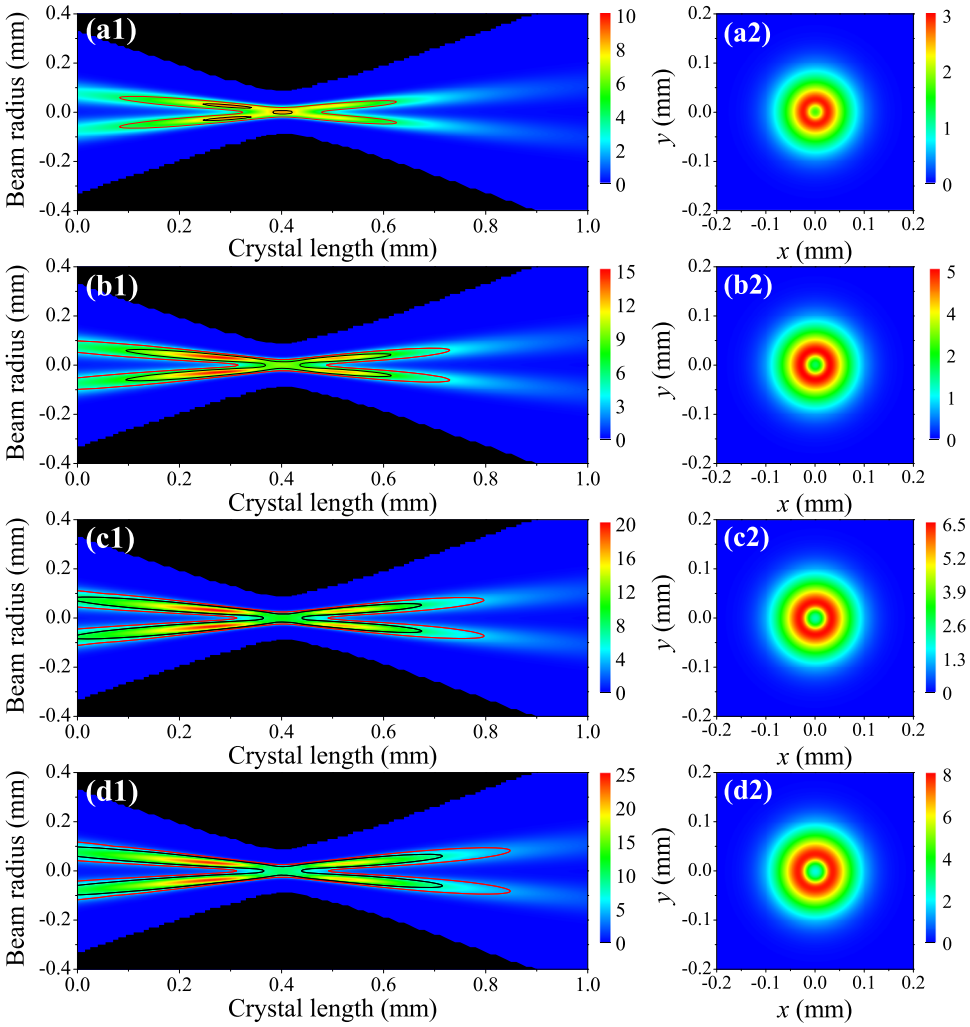

FIG. 4. Theoretically calculated saturated population inversion distribution (a1)–(d1) and effective population inversion distribution (a2)–(d2) along the 1-mm-thick Yb:YAG crystal under a focused annular beam pumping for different incident pump powers: the focus spot locates at 0.4 mm respective to the entrance surface of the Yb:YAG crystal. (a) P_{in} = 2 W, (b) P_{in} = 4 W, (c) P_{in} = 6 W, and (d) P_{in} = 8 W. The solid red lines are the contour lines with a value of 4, and the solid black lines are the contour lines with values of 8. The unit of the population inversion is $\times 10^{20}$ cm^{-3}.

of P_{in} on the population inversion distribution. The pumped region with population inversion higher than 4×10^{20} cm^{-3} at P_{in} = 2 W is from 0.08 mm to 0.63 mm inside the Yb:YAG crystal. The pumped region with population inversion higher than 8×10^{20} cm^{-3} is from 0.245 mm to 0.34 mm and a small portion centered at focus spot, as shown in Fig. 4(a1). The pumped region with population inversion higher than 4×10^{20} cm^{-3} around focus spot is possible for supporting TEM_{00} mode oscillation; however, the effective gain length is short (0.16 mm, from 0.32 mm to 0.48 mm); therefore, this pumped region cannot support TEM_{00} mode oscillation in the Yb:YAG microchip laser. This pumped region with population inversion around focus spot acts as a intracavity saturable loss for $LG_{0,l}$ modes because the spatial distribution of the saturable loss depends on the spatial distribution of $LG_{0,l}$ mode laser field. Thus, only $LG_{0,l}$ mode laser oscillates in the Yb:YAG microchip laser under annular beam pumping, which is in good agreement with the experimentally observed $LG_{0,l}$ mode laser. Further increase in P_{in}, the pumped region with population inversion higher than 4×10^{20} cm^{-3} is expanded. As shown in Fig. 4(b1), at P_{in} = 4 W, the pumped region with population inversion higher than 4×10^{20} cm^{-3} is expanded from 0 to 0.73 mm. Also, the pumped region with population inversion higher than 8×10^{20} cm^{-3} is enlarged from 0.1 mm to 0.62 mm. The beam area along the radial direction is also expanded, and the pumped region around focus spot induced saturable loss for the $LG_{0,l}$ mode laser with small l is increased, which is more favorable for the $LG_{0,l}$ mode laser with large l. Therefore, an increase in the gain for the $LG_{0,l}$ mode laser with large l and the saturable loss for the $LG_{0,l}$ mode laser with small l make the $LG_{0,l}$ mode laser with large l preferable to oscillate. The population inversion increases with the pump power, as shown in Figs. 4(c1) and 4(d1), the unpumped and the pumped regions below-threshold exhibit reabsorption loss and act as spatial filter for choosing $LG_{0,l}$ mode lasers. The pump regions around focus spot (e.g., from 0.3 mm to 0.5 mm) cannot support TEM_{00} mode oscillation owing to the short gain region (about 0.2 mm), which acts as a saturable loss for $LG_{0,l}$ mode lasers. This spatial dependent saturable loss depends on the on-axis population inversion distribution, which relays on the applied pump power.

The effective saturated population inversion distribution at different P_{in}s is shown in Figs. 4(a2)–4(d2). The effective saturated population inversion distribution at different P_{in}s is a donut shape. The effective saturated population inversion at the pumped regions around the optical axis is lower at the ring because the position-dependent population inversion induced by the annular beam contributes more from two pumped regions away from focus spot than that achieved around the focus spot, as shown in Fig. 4(a1). This is caused by the exponential decay of the absorbed pump power along the Yb:YAG crystal length and pump power saturation effect under tightly pumping. As shown from Figs. 4(a2)–4(d2), the inner diameter of the ring with highest population inversion increases with P_{in}. The pumped region with sufficient population inversion is expanded and population inversion increases with P_{in}. Therefore, the saturable loss caused by the pumped regions below threshold for low order $LG_{0,l}$ mode increases, while the population inversion achieved at a high pump power is favorable for generating a high order $LG_{0,l}$ mode laser.

Formation of the pump power-dependent vortices with tunable topological charges in an annular beam pumped Yb:YAG microchip laser is attributed to the aperture guiding effect and reabsorption loss of the quasi-three-level Yb:YAG crystal. Suppression of TEM_{00} mode oscillation is achieved by a tightly focused annular beam with a short Raleigh range. The pumped regions around focus spot act as saturable losses for the $LG_{0,l}$ mode. The pump power-dependent saturated population inversion distribution around focus spot is calculated and shown in Fig. 5. The population inversion excited at the pumped region around focus spot from 0.3 mm to 0.5 mm cannot support the TEM_{00} mode oscillation because the effective gain length is only 0.2 mm. Therefore, this pumped region is acted as a reabsorption loss for $LG_{0,l}$ modes. In the Yb:YAG microchip laser, the unpumped region and pumped region below-threshold exhibit reabsorption loss and act as a spatial filter for selecting transverse modes. For the pump beam with a focused annular profile as shown in Fig. 1, the distribution of population inversion at focus spot (z = 0.4 mm) is a super-Gaussian profile, as shown in Fig. 5(b). The population inversion increases, and the gain region expands with P_{in}. However, the saturated population inversion increases only 20% when P_{in} increases from 2 W to 8 W. This is caused by the high pump power intensity induced pump saturation effect. The population inversion around focus spot tends to decrease along the beam axis and expands along the radial direction, as shown in Figs. 5(a) and 5(c). At low pump power, e.g., P_{in} = 2 W, the two-peak population inversion decreases away from focus spot. At high pump power, e.g., P_{in} = 4 W or higher, the population inversion increases with P_{in} and tends to expand, as shown in Figs. 5(a) and 5(c). This gain guiding effect is caused by the pump power intensity saturation effect. The pump power-depending population inversion distribution around focus spot has two effects on the formation of $LG_{0,l}$ modes depending on applied pump power. One is that the pumped region around focus spot acts as a reabsorption loss to the $LG_{0,l}$ modes, and the other is that the off-axis population inversion around two peaks further increases saturable loss for the low-order LG mode and support the laser oscillation of high-order $LG_{0,l}$ modes. As shown in Figs. 4 and 5, the pump power dependent population inversion distribution inside the Yb:YAG crystal plays a key role on formation of vector-vortex beams with different topological charges. Therefore, $LG_{0,l}$ vector-vortex lasers with tunable topological charges have been generated in the annular beam pumped Yb:YAG microchip laser depending on the applied pump power.

In order to verify the beam propagation quality of these $LG_{0,l}$ mode lasers obtained in the annular beam pumped Yb:YAG microchip laser, the beam quality factor, M^2, of different $LG_{0,l}$ mode lasers was obtained by measuring the beam radii along the beam propagation direction. The beam radius of the $LG_{0,l}$ mode lasers measured in the experiments was defined in terms of the $1/e^2$ intensity points of the outermost lobe. The position dependent beam radius for $LG_{0,l}$ modes (l = 1, 7, 10, 14) are shown in Fig. 6(a). The M^2 values were obtained by fitting the data with the beam propagation formula of the $LG_{0,l}$ mode laser. The M^2 values of $LG_{0,1}$, $LG_{0,7}$, $LG_{0,10}$, and $LG_{0,14}$ modes were fitted to be 2.11, 8.47, 11.17, and 15.14, respectively, which are nearly equal to the theoretical values of $M^2 = l + 1$ for $LG_{0,l}$ modes (e.g., 2 for $LG_{0,1}$ mode, 8 for $LG_{0,7}$ mode, 11 for $LG_{0,10}$ mode, and 15 for $LG_{0,14}$ mode). The measured M^2 values for obtained $LG_{0,l}$ mode lasers with l from 1 to 14 are shown in Fig. 6(b), together with the theoretically calculated M^2 values of $LG_{0,l}$ modes. The obtained M^2 values for $LG_{0,l}$ modes (l = 1, 2, . . ., 14) in the Yb:YAG microchip laser are nearly equal to the theoretically calculated M^2 values, which indicates that the diffraction-limited beam quality has been achieved for $LG_{0,l}$ (l = 1, 2, . . ., 14) vector-vortex beams generated in the annular beam pumped microchip laser.

The phases of the $LG_{0,l}$ donut-shaped transverse mode lasers have been checked by self-interfering with a plane-wave reference beam obtained from the $LG_{0,l}$ mode laser. The $LG_{0,l}$ mode laser beam generated in the Yb:YAG microchip laser was separated to form a plane wave reference beam with an aperture. Then, the original laser beam from the Yb:YAG microchip laser and the reference

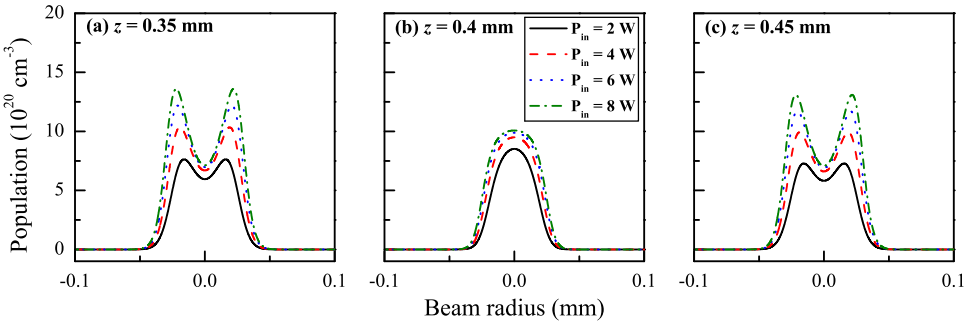

FIG. 5. Population inversion distribution inside the Yb:YAG crystal around the focus spot for different pump powers: (a) z = 0.35 mm, (b) z = 0.4 mm, and (c) z = 0.45 mm.

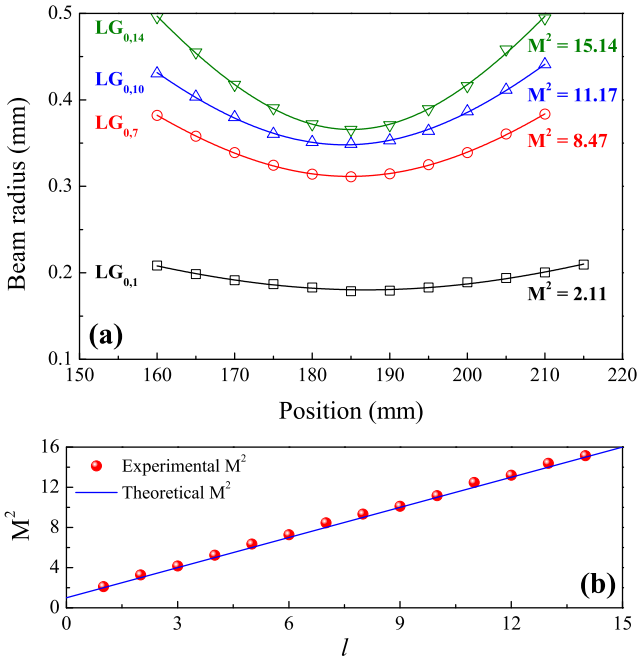

FIG. 6. (a) Measured beam radius as a function of the position for $LG_{0,l}$ (l = 1, 7, 10, 14) vector-vortex beams after focusing with a lens. Solid lines are theoretical fits with the beam propagation expression of $LG_{0,l}$ (l = 1, 7, 10, 14) modes. (b) Measured beam quality factor, M^2, as a function of the order of $LG_{0,l}$ vector-vortex beams, l. The solid line is the theoretically calculated M^2 for different orders of $LG_{0,l}$ modes.

beam were interfered on a charge-coupled device (CCD). The interference patterns obtained for $LG_{0,l}$ vortex beams with l up to 10 are shown in Fig. 7. The corresponding theoretical simulations of the interference patterns of $LG_{0,l}$ modes with a plane wave reference beam are performed and also shown in Fig. 7. It clearly shows that one interference fringe splits to two fringes at forklike dislocation for the $LG_{0,1}$ vortex beam. The forklike interference pattern provides a clear evidence that the output $LG_{0,1}$ donut-shaped beam is an optical vortex with helical wave-front and topological charge $l = 1$. This is to say, the helical phase of the obtained $LG_{0,1}$ mode laser confirms that it is a vortex beam carrying OAM. Similarly, one interference fringe splits to $l + 1$ fringes at the forklike dislocation for a $LG_{0,l}$ vortex beam, as shown in Fig. 7. There are some discrepancies between measured and theoretically calculated interference patterns of the $LG_{0,l}$ ($l \geq 5$) vortex beams with a plane-wave reference beam. There is a bright spot at the center of the measured interference patterns for $LG_{0,l}$ vortex beams ($l \geq 5$). This is caused by the large beam area plane-wave reference beam at the focal plane required for interfering with high-order $LG_{0,l}$ vortex beams ($l \geq 5$). Because the $LG_{0,l}$ vector-vortex beams generated in the Yb:YAG microchip laser were inhomogeneous polarized, a focus lens with large focal length was used to maintain hollow structure at the focal plane; therefore, the focal spot of the $LG_{0,l}$ vector-vortex beam was large. For fulfilling the interference condition, a large beam area plane-wave reference beam with certain intensity is required. Thus, there is a bright spot at the center of the interference patterns. Even with some imperfections, the experimentally obtained interference patterns of the $LG_{0,l}$ mode lasers are in fair agreement with theoretical simulated interference patterns, which gives a clear evidence that the obtained $LG_{0,l}$ donut-shaped beams in the annular beam pumped Yb:YAG microchip laser

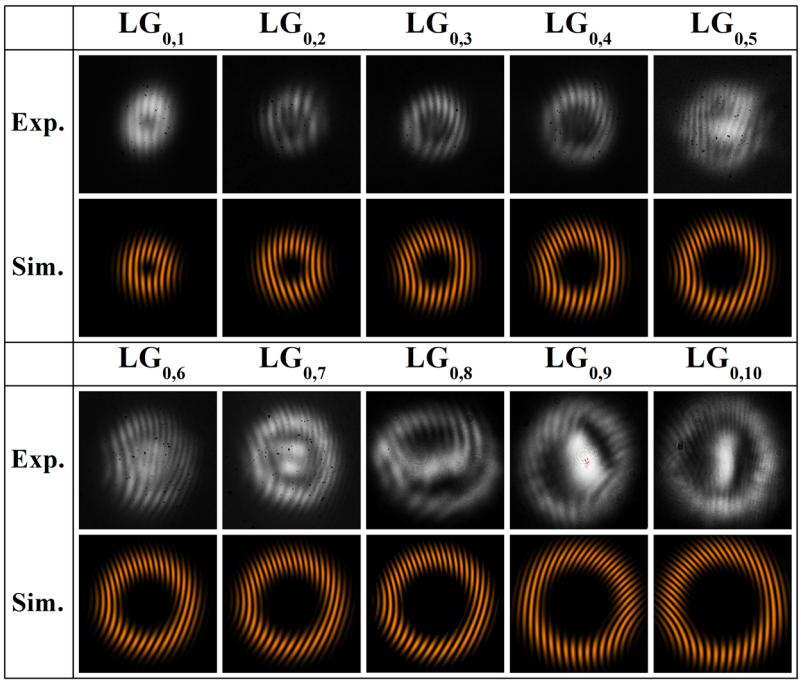

FIG. 7. Measured and theoretically calculated interference patterns of $LG_{0,l}$ (l = 1,2, . . ., 10) vortex beams with a plane-wave reference beam.

are vortex beams with tunable topological charges. The obtained vortex beams carry tunable OAM depending on the applied pump power.

B. Polarization states of $LG_{0,l}$ vector-vortex beams

The polarization states of $LG_{0,l}$ vector-vortex beams with tunable topological charges were evaluated by passing the vector-vortex laser beams through a linear polarizer. Experimentally obtained polarization patterns of $LG_{0,l}$ vector-vortex beams together with theoretically simulated polarization patterns of the $LG_{0,l}$ vector-vortex laser are shown in Fig. 8. The two-lobe polarization pattern was observed when the $LG_{0,1}$ vector-vortex beam passed through a linear polarizer, as shown in Fig. 8(a). The two-lobe polarization pattern was kept with rotation of the polarizer. Four lobes were observed when a $LG_{0,2}$ vector-vortex beam passed through a linear polarizer, as shown in Fig. 8(b). Similarly, when a $LG_{0,l}$ vector-vortex beam passes through a linear polarizer, the polarization pattern with $2l$ lobes is observed, for example, 28 lobes are obtained for the $LG_{0,14}$ vector-vortex beam, as shown in Fig. 8(n). The obtained $2l$-lobe polarization patterns for $LG_{0,l}$ vector-vortex beams rotate in the same direction with the rotation of the polarizer, which indicates the obtained $LG_{0,l}$ vortex beams are vector-vortex beams with cylindrical polarization distribution depending on the order of $LG_{0,l}$ modes. Good agreement is achieved between experimentally obtained polarization patterns of the vector-vortex beams with tunable topological charges and theoretically calculated polarization patterns of $LG_{0,l}$ vector-vortex beams with cylindrical polarization distribution, as shown in Fig. 8. Therefore, high-order cylindrical vector beams with tunable topological charge from 1 to 14 have been achieved in an annular beam pumped Yb:YAG microchip laser.

Figure 9 gives some examples of experimentally obtained polarization patterns at different rotation angles of the linear polarizer. When a $LG_{0,1}$ vector-vortex beam passes through a linear polarizer, the two-lobe pattern is observed. The two-lobe patterns are kept and rotated clockwise in the same speed as the rotation of the polarizer, which indicates that the experimentally obtained $LG_{0,1}$ vector-vortex beam is radially polarized, as shown in Fig. 9(a). The six-lobe pattern was observed when a $LG_{0,3}$ vector-vortex beam passed through a linear polarizer, and the six-lobe pattern was kept and rotated with rotating the linear polarizer, as shown in Fig. 9(b). However, the rotation angle of the six-lobe polarization pattern was just one third of the rotation angle of the polarizer. As shown in Fig. 9(c), the twelve-lobe polarization pattern was observed when a $LG_{0,6}$ vector-vortex beam passed through a linear polarizer. The twelve-lobe polarization pattern rotated in the same way as the rotation of the linear polarizer. The rotation angle of the twelve-lobe polarization pattern was one sixth of the rotation angle of the polarizer. The number of lobes and rotation angle of the polarization pattern for $LG_{0,l}$ vector-vortex beams are $2l$ and ϕ/l for the rotation angle ϕ of the polarizer. Although the rotation angle of polarization patterns is ϕ/l for $LG_{0,l}$ vector-vortex beams, the rotation of the polarization pattern coincident with the rotation of the polarizer clearly indicates that the experimentally obtained $LG_{0,l}$ vortex beams in the annular beam pumped Yb:YAG microchip laser are high-order cylindrical vector beams. The electric fields of the experimentally obtained $LG_{0,l}$ vector-vortex beams can be expressed as[19,32]

$$\vec{E}_{0l}(r,\phi) = \sqrt{\frac{2}{\pi}}\left(\frac{1}{l!}\right)^{1/2}\left(\frac{2r^2}{w_0^2}\right)^{l/2}\exp\left(\frac{-r^2}{w_0^2}\right) \times \left[\sin(l-1)\phi\cdot\vec{P}_\phi + \cos(l-1)\phi\cdot\vec{P}_r\right], \quad (8)$$

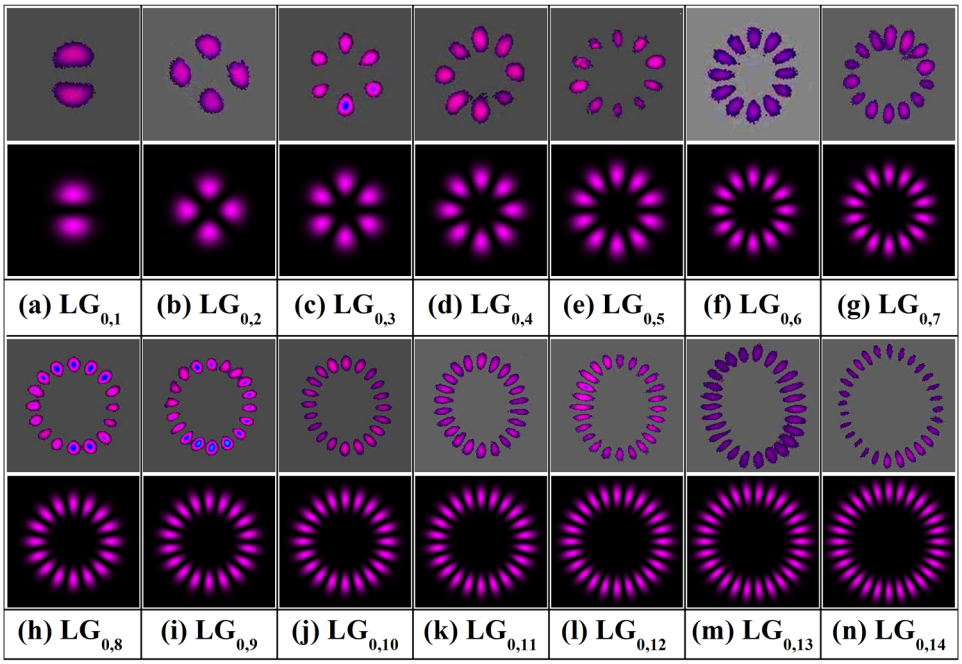

FIG. 8. Experimental obtained and theoretical simulated polarization patterns of $LG_{0,l}$ vector-vortex beams after passing through a linear polarizer. (a) $LG_{0,1}$. (b) $LG_{0,2}$. (c) $LG_{0,3}$. (d) $LG_{0,4}$. (e) $LG_{0,5}$. (f) $LG_{0,6}$. (g) $LG_{0,7}$. (h) $LG_{0,8}$. (i) $LG_{0,9}$. (j) $LG_{0,10}$. (k) $LG_{0,11}$. (l) $LG_{0,12}$. (m) $LG_{0,13}$. (n) $LG_{0,14}$.

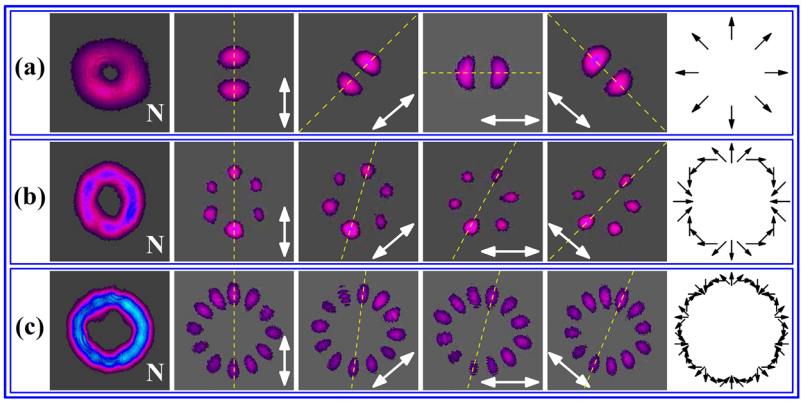

FIG. 9. Typical total transverse patterns and polarization patterns at the rotation angle of the polarizer (0°, 45°, 90°, and 135°) after passing through a linear polarizer for three $LG_{0,l}$-based vector-vortex beams obtained in the Yb:YAG microchip laser (a) $LG_{0,1}$, (b) $LG_{0,3}$, and (c) $LG_{0,6}$, respectively. "N" indicates the total transverse patterns of vector-vortex beams. The solid arrows show the rotation angles of the linear polarizer. The dashed lines indicate the rotation angles of polarization patterns. The corresponding polarization distributions are shown with the vector field plots in the last column.

where r and ϕ are the radial and azimuthal coordinates and $\vec{P}_r$ and $\vec{P}_\phi$ are the unit vectors of electric fields for radial and azimuthal directions, respectively.

The mechanism of generating vector-vortex beams with cylindrical polarization distribution in the annular beam pumped Yb:YAG microchip laser is attributed to the thermal-induced bifocusing effect in the Yb:YAG crystal. For the isotropic Yb:YAG crystal similar to the Nd:YAG crystal, the thermal lenses induced by the thermally induced birefringence are different for the radially and azimuthally polarized beams in end-pumped solid-state lasers.[33] Therefore, two different focal points appear for radial and azimuthal polarization components. For the present annular beam pumped Yb:YAG microchip laser, the annular pump beam can be treated as superposition of infinite Gaussian beams (local pump beam), as described in the Nd:YAG microchip laser.[24] The pump power dependent local laser beam radii along radial and azimuthal directions induced by the inhomogeneous local Gaussian pump beams have been calculated theoretically based on the thermal lens expression.[24] The absorption coefficient of 10 cm^{-1} and thermal loading of 0.11 for the Yb:YAG crystal were used in theoretical calculation. Other parameters used in theoretical calculation were taken from Refs. 34 and 24. As shown in Fig. 10, the theoretically calculated local laser beam radius along the radial direction is smaller than that along the azimuthal direction when the pump power was less than 15 W. The overall coupling efficiency for the radially polarized mode is higher than that for the azimuthally polarized mode when the incident pump power is less than 15 W. Therefore, the radially polarized mode starts to oscillate first and fully extracts the energy stored in the gain medium, while the azimuthally polarized mode is suppressed. The incident pump power of 15 W for radial polarized mode oscillation in the Yb:YAG microchip laser is higher than that for the Nd:YAG microchip laser,[24] which is attributed to that the thermal loading of the Yb:YAG crystal is only one third of that of the Nd:YAG crystal.[35]

Degree of polarization (DOP) is an important parameter to evaluate purity of the polarization state of high-order cylindrical vector beam. The DOP of the cylindrically polarized vector-vortex lasers with tunable topological charges was obtained by measuring

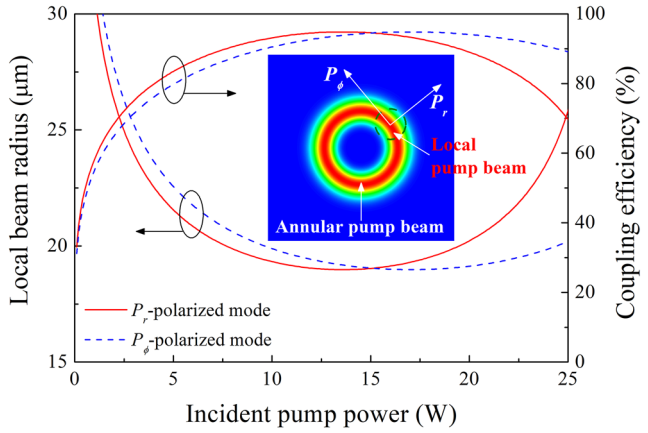

FIG. 10. Local laser beam radii and the corresponding coupling efficiencies with local pump beam radius for radially (P_r) and azimuthally (P_ϕ) polarized laser modes as a function of incident pump power. Inset: schematic of the distribution of the annular pump beam incident on the Yb:YAG crystal. The dashed circle denotes one local pump beam divided from the annular pump beam.

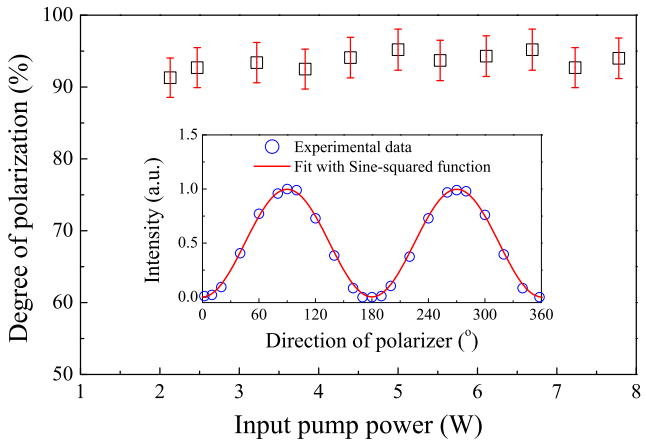

FIG. 11. Degree of polarization of obtained $LG_{0,l}$ vector-vortex lasers as a function of P_{in}. The inset is the measured power of the selected tiny beam from a vector-vortex laser beam passing a linear polarizer as a function of the polarizer direction, and the solid line is the fitting curve with a sine-squared function.

the polarization state of any portion of the donut vortex beam profile. In the experiment for measuring DOP, a tiny portion of the beam was selected from a $LG_{0,l}$ vector-vortex beam with an aperture. Then, the output power passing through a linear polarizer was measured at different angles of the linear polarizer. The inset of Fig. 11 shows the polarizer direction-dependent power of the selected beam at P_{in} = 7.8 W. The experimentally measured polarizer direction-dependent laser power was fitted very well with the sine-squared function, which provides a strong evidence of the polarization states of any tiny portion of the vortex beam is linear polarization. The DOP was obtained with the expression $(P_{max} - P_{min})/(P_{max} + P_{min})$, where P_{max} and P_{min} were the maximum and minimum values of the fitted curve, respectively. Figure 11 shows the measured DOP of the vector-vortex lasers with tunable topological charges as a function of P_{in}. Although there is a small fluctuation in DOP with P_{in}, the DOP remains over 91% with increasing P_{in}. Therefore, the high polarization purity has been achieved in the cylindrically polarized vector-vortex lasers with tunable topological charges.

C. Laser spectra of vector-vortex lasers

The laser spectra of vector-vortex lasers with tunable topological charges have been carefully measured. The central wavelength is around 1030 nm at pump power less than 4.5 W, the lasing wavelength shifts to longer wavelength, and dual-wavelength (1030 and 1050 nm) is obtained at pump power between 4.5 W and 6.3 W. The lasing wavelength shifts to 1050 nm at pump power higher than 6.5 W. Figure 12 shows some laser spectra of the $LG_{0,l}$ vector-vortex lasers at different P_{in}s. The vector-vortex laser with one topological charge oscillates around 1030 nm with 9 longitudinal modes at P_{in} = 2.1 W, as shown in Fig. 12(a). The vector-vortex lasers with topological charge from 2 to 7 oscillate at 1030 nm, and the longitudinal modes increase to 12 as P_{in} increases to 4.5 W. Further increase in P_{in} from 4.5 W to 6.3 W, the vector-vortex lasers with topological charge of 8, 9, and 10 oscillate at dual-wavelength (1030 and 1050 nm), as shown in Figs. 12(b)–12(d). As P_{in} increases from 4.5 W to 6.3 W, the intensity and number of the longitudinal modes around 1030 nm decrease, while the intensity and number of the longitudinal modes around 1050 nm increase. When P_{in} is higher than 6.3 W, the vector-vortex laser oscillates only around 1050 nm, as shown in Fig. 12(e). The wavelength shift and dual-wavelength oscillation of vector-vortex lasers are caused by the temperature dependent emission spectrum of the Yb:YAG crystal,[26] and the enhanced reabsorption at 1030 nm due to the aggressive thermal accumulation induced temperature rise with pump power. Because the OC with high reflectivity was used in the experiment, the reabsorption loss at 1030 nm is the main factor for suppressing 1030 nm laser oscillation. The separation between two adjacent longitudinal modes was measured to be 0.28 nm and 0.29 nm for 1030 nm and 1050 nm, respectively, which are in good agreement with the free spectral range (0.29 nm for 1030 nm and 0.303 nm for 1050 nm) of axial modes in the 1-mm-thick Yb:YAG resonator. The linewidth of the longitudinal mode is less than 0.03 nm, which is limited by the resolution of the optical spectral analyzer.

D. Performance of $LG_{0,l}$ vector-vortex laser

Figure 13 shows the output power of the $LG_{0,l}$ vector-vortex Yb:YAG microchip laser as a function of P_{in}. The threshold pump power of the annular beam pumped Yb:YAG microchip laser was 1.85 W. The output power increases with P_{in}. The slope efficiency is 9.2% when P_{in} is lower than 3.9 W. The slope efficiency is 23.2% when P_{in} is between 3.9 W and 6.3 W and is 39.3% when P_{in} is higher than 6.3 W. An increase in the slope efficiency is attributed to an increase in the pump power intensity. High pump power intensity causes extensive competition between $LG_{0,l}$ transverse modes and competition for the gain at oscillating wavelengths (1030 and 1050 nm). High pump power intensity is favorable for efficient operation of the Yb:YAG laser.[36] Because the focused annular beam was used in the experiment, the pump power saturation induced gain guiding effect has to be considered at the focus spot. The gain guiding effect contributes more to expand the pump beam area with an increase in P_{in}. The expanding of the pump beam induced saturation inversion around the focal spot makes $LG_{0,l}$ modes with large l preferable to oscillate.

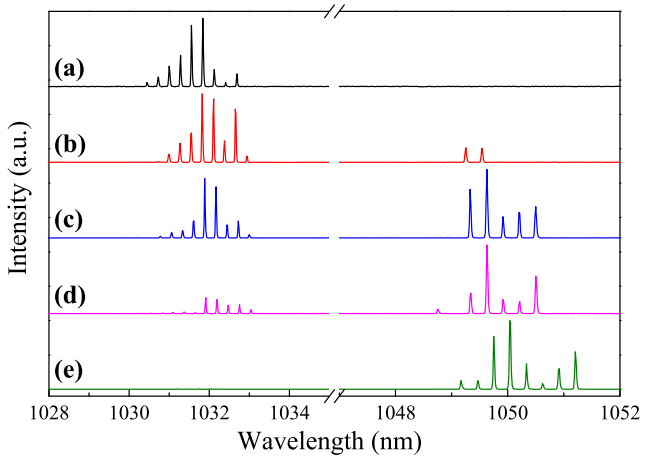

FIG. 12. Laser emitting spectra of vector-vortex lasers with different topological charges at different incident pump powers: (a) P_{in} = 2.1 W, (b) P_{in} = 5 W, (c) P_{in} = 5.5 W, (d) P_{in} = 6.1 W, and (e) P_{in} = 6.7 W.

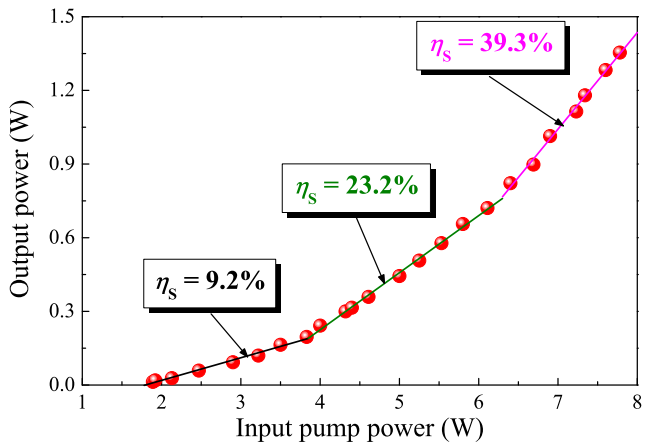

FIG. 13. Output power of the vector-vortex laser with tunable topological charge as a function of P_{in}. The solid lines are linear fits of the experimental data.

Because the annular pump beam area with sufficient population inversion expands as P_{in} increases, the high order $LG_{0,l}$ mode is favorable to oscillate. Therefore, the output power of the $LG_{0,l}$ vortex laser with large l increases with a high slope efficiency at a high pump power level. Four high order vector-vortex lasers ($LG_{0,11}$, $LG_{0,12}$, $LG_{0,13}$, and $LG_{0,14}$) with an output power of over 1 W have been obtained in the Yb:YAG microchip laser. The maximum output power is 1.36 W for the $LG_{0,14}$ vector-vortex laser at P_{in} = 7.8 W. The optical-to-optical efficiency is 17.5%, which is about 3.5 times of that achieved in a Nd:YVO_4 laser with inscribed round patterns on an output coupler.[20] There is no output power rollover observed at maximum available pump power, which indicates that the output power can be further scaled by applying high pump power. The higher order $LG_{0,l}$ ($l > 14$) vector-vortex beams with a high output power are possible by applying high pump power. The threshold pump powers for $LG_{0,l}$ vector-vortex lasers increase with the order of $LG_{0,l}$ vector-vortex beams generated in the Yb:YAG microchip laser because the diffraction loss and reabsorption loss of the $LG_{0,l}$ mode increase with l. The range of incident pump power for stable oscillation of a particular $LG_{0,l}$ vector-vortex beam is larger than 0.3 W, which indicates that this annular beam pumped microchip laser is a flexible and robust laser source for generating distinct polarized vector-vortex beams with tunable topological charges.

With the parameters of the focused annular beam end-pumped Yb:YAG microchip laser: w_{p0} = 20 μm, θ_p = 10°, α = 10 cm^{-1}, L_c = 1 mm, ν_p = 3.19 × 10^{14} Hz, $\eta_a = 1 - \exp(-\alpha L_c)$, and z_0 = 0.4 mm, the threshold pump powers for $LG_{0,l}$ modes with different topological charges were calculated with Eq. (6). The theoretically calculated threshold pump powers of $LG_{0,l}$ mode lasers oscillating at 1030 and 1050 nm for different topological charge numbers are plotted in Fig. 14. The threshold pump powers for 1030 and 1050 nm laser oscillation increase with the topological charges. However, the threshold pump powers for the 1030 nm laser are lower than those for the 1050 nm laser when the topological charge number is less than 7; therefore, the optical vortices with topological charges less than 7 oscillates preferable at 1030 nm. The threshold pump powers for the 1030 nm laser are higher than those for the 1050 nm laser when the topological charge number is larger than 7 because aggressive re-absorption loss at 1030 nm plays a dominant role to balance the net gain for 1030 and 1050 nm laser oscillation. The theoretically calculated thresholds pump powers for optical vortices with different topological charges are in good agreement with experimental data, as shown in Fig. 14. The shift of laser wavelength from 1030 nm to 1050 nm is attributed to the enhanced reabsorption loss of the Yb:YAG crystal at 1030 nm. The reabsorption loss of the Yb:YAG microchip laser is proportional to the laser beam area of the $LG_{0,l}$ mode laser which increases with the topological charge. Although the emission cross section at 1050 nm is about one sixth of that at 1030 nm for the Yb:YAG crystal, the reabsorption loss at 1050 nm is far less than that at 1030 nm. The emission cross section at laser wavelength decreases, and the absorption coefficient at 1030 nm increases with a temperature rise induced by the thermal accumulation at the high pump power. Therefore, there is a balance for gain and loss between 1030 and 1050 nm laser oscillations, which determines the laser oscillating wavelength.

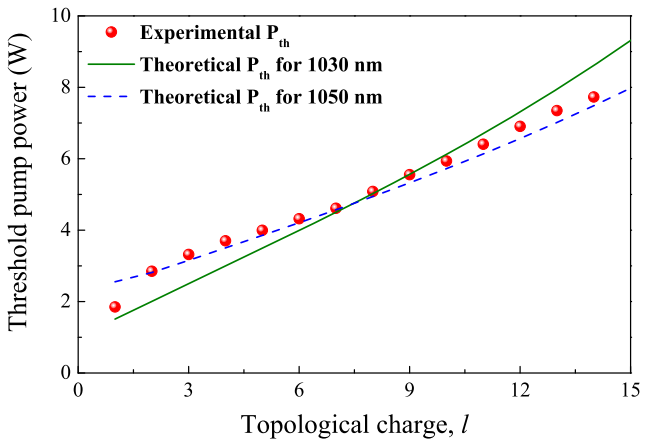

FIG. 14. Experimental threshold pump powers (solid dots) and theoretically calculated threshold pump powers (lines) for 1030 nm and 1050 nm laser oscillation as a function of topological charges.

The discrepancies between measured threshold pump powers and the theoretically calculated threshold pump powers for optical vortices with different topological charges are attributed to inaccurate estimation of the intracavity losses in the theoretical calculations. Also the pump power dependent thermal effect of gain medium is not considered in the theoretical calculation; the pump power dependent thermal effect changes the optical properties of the Yb:YAG crystal such as broadening optical spectra and decreasing the absorption coefficient and emission cross section, which dramatically increase the threshold pump power for laser oscillation.

V. CONCLUSIONS

In conclusion, high beam quality, high-order cylindrical vector beams with tunable topological charge have been demonstrated in an annular beam pumped Yb:YAG microchip laser. Vortices with topological charge tuning from 1 to 14 have been achieved by adjusting the incident pump power. Vector-vortex lasers with topological charge from 1 to 7 oscillate at 1030 nm. Vector-vortex lasers with topological charge from 8 to 10 work at 1030 and 1050 nm dual-wavelength. Vector-vortex lasers with topological charge from 11 to 14 work at 1050 nm. The intensity patterns and experimental interference patterns of vector-vortex beams observed agree with theoretical predictions. The helical phases of the topological charge tunable vector-vortex beams are stable and reproducible once the laser oscillation is established. The output power of 1.36 W has been achieved for the vector-vortex laser with 14 topological charges, and the optical efficiency is 17.5%. High beam quality has been achieved for high-order cylindrical vector beams with tunable topological charges. This work provides a flexible and robust method for generating high beam quality, wavelength tunable and topological charge tunable high-order cylindrical vector beams in compact solid-state lasers, which have potential applications on information processing and storage, laser material processing, and integrated optics.

ACKNOWLEDGMENTS

This work was supported by the National Natural Science Foundation of China (Grant Nos. 61275143 and 61475130) and the

Fundamental Research Funds for the Central Universities (Grant No. 20720192020).

REFERENCES

[1]J. Wang, J. Y. Yang, I. M. Fazal, N. Ahmed, Y. Yan, H. Huang, Y. X. Ren, Y. Yue, S. Dolinar, M. Tur, and A. E. Willner, Nat. Photonics **6**(7), 488 (2012).
[2]G. Gibson, J. Courtial, M. J. Padgett, M. Vasnetsov, V. Pas'ko, S. M. Barnett, and S. Franke-Arnold, Opt. Express **12**(22), 5448 (2004).
[3]R. Fickler, R. Lapkiewicz, W. N. Plick, M. Krenn, C. Schaeff, S. Ramelow, and A. Zeilinger, Science **338**(6107), 640 (2012).
[4]Y. Kozawa, D. Matsunaga, and S. Sato, Optica **5**(2), 86 (2018).
[5]D. G. Grier, Nature **424**(6950), 810 (2003).
[6]L. Allen, M. W. Beijersbergen, R. J. C. Spreeuw, and J. P. Woerdman, Phys. Rev. A **45**(11), 8185 (1992).
[7]R. Dorn, S. Quabis, and G. Leuchs, Phys. Rev. Lett. **91**(23), 233901 (2003).
[8]Q. W. Zhan, Adv. Opt. Photonics **1**(1), 1 (2009).
[9]C. Rosales-Guzman, B. Ndagano, and A. Forbes, J. Opt. **20**(12), 123001 (2018).
[10]R. Fickler, G. Campbell, B. Buchler, P. K. Lam, and A. Zeilinger, Proc. Natl. Acad. Sci. U. S. A. **113**(48), 13642 (2016).
[11]S. Ngcobo, I. Litvin, L. Burger, and A. Forbes, Nat. Commun. **4**, 2289 (2013).
[12]C. Maurer, A. Jesacher, S. Fürhapter, S. Bernet, and M. Ritsch-Marte, New J. Phys. **9**(3), 78 (2007).
[13]F. Ricci, W. Loffler, and M. P. van Exter, Opt. Express **20**(20), 22961 (2012).
[14]K. Huang, P. Shi, G. W. Cao, K. Li, X. B. Zhang, and Y. P. Li, Opt. Lett. **36**(6), 888 (2011).
[15]K. Yonezawa, Y. Kozawa, and S. Sato, Jpn. J. Appl. Phys., Part 1 **46**(8A), 5160 (2007).
[16]S. N. Khonina, S. V. Karpeev, S. V. Alferov, and V. A. Soifer, J. Opt. **17**(6), 065001 (2015).
[17]Y. Kozawa and S. Sato, Opt. Lett. **30**(22), 3063 (2005).
[18]M. A. Ahmed, A. Voss, M. M. Vogel, and T. Graf, Opt. Lett. **32**(22), 3272 (2007).
[19]A. Ito, Y. Kozawa, and S. Sato, J. Opt. Soc. Am. A **27**(9), 2072 (2010).
[20]Z. Qiao, G. Q. Xie, Y. H. Wu, P. Yuan, J. G. Ma, L. J. Qian, and D. Y. Fan, Laser Photonics Rev. **12**(8), 1800019 (2018).
[21]J. W. Kim, J. I. Mackenzie, J. R. Hayes, and W. A. Clarkson, Opt. Express **19**(15), 14526 (2011).
[22]Z. Q. Fang, K. G. Xia, Y. Yao, and J. L. Li, Appl. Phys. B **117**(1), 219 (2014).
[23]M. D. Wei, Y. S. Lai, and K. C. Chang, Opt. Lett. **38**(14), 2443 (2013).
[24]H. S. He, Z. Chen, and J. Dong, Appl. Phys. Express **10**(5), 052701 (2017).
[25]D. M. Chen, X. C. Wang, H. S. He, and J. Dong, Appl. Phys. Express **12**(5), 052012 (2019).
[26]J. Dong, M. Bass, Y. L. Mao, P. Z. Deng, and F. X. Gan, J. Opt. Soc. Am. B **20**(9), 1975 (2003).
[27]J. Dong, A. Shirakawa, K. Ueda, H. Yagi, T. Yanagitani, and A. A. Kaminskii, Appl. Phys. Lett. **89**(9), 091114 (2006).
[28]S. S. Stafeev, V. V. Kotlyar, A. G. Nalimov, and E. S. Kozloval, IEEE Photonics J. **11**(4), 4500810 (2019).
[29]K. Kubodera, K. Otsuka, and S. Miyazawa, Appl. Opt. **18**(6), 884 (1979).
[30]L. V. Vainshtein, J. Exp. Theor. Phys. **17**(3), 709 (1963).
[31]D. Kawase, Y. Miyamoto, M. Takeda, K. Sasaki, and S. Takeuchi, Phys. Rev. Lett. **101**(5), 050501 (2008).
[32]A. A. Tovar, J. Opt. Soc. Am. A **15**(10), 2705 (1998).
[33]G. Machavariani, Y. Lumer, I. Moshe, A. Meir, S. Jackel, and N. Davidson, Appl. Opt. **46**(16), 3304 (2007).
[34]W. Koechner, Appl. Opt. **9**(11), 2548 (1970).
[35]T. Y. Fan, IEEE J. Quantum Electron. **29**(6), 1457 (1993).
[36]J. Dong and K. Ueda, Laser Phys. Lett. **2**(9), 429 (2005).